Contents lists available at ScienceDirect

Transactions of Nonferrous Metals Society of China

36(2026) 25−42

www.tnmsc.cn

Quantitative analysis on *T*1 phase precipitation behaviors and mechanical properties of 2195 Al−Li alloy after cryogenic deformation and aging

Meng-jia YAO [a,b], Hua-bo ZHOU [a,b], Rui-qian WANG [a,b], Wei LIU [a,b,*]

[a] National Key Laboratory for Precision Hot Processing of Metals, Harbin Institute of Technology, Harbin 150001, China;

[b] School of Materials Science and Engineering, Harbin Institute of Technology, Harbin 150001, China

---

Abstract: The water-quenched (WQ) 2195 Al−Li alloy was subjected to stretching at different temperatures, from room temperature (RT) to −196 °C (CT), to investigate the effect of cryogenic deformation on the aging precipitation behaviors and mechanical properties. The precipitation kinetics of the *T*1 phase and the microstructures in peak aging state were investigated through the differential scanning calorimetric (DSC) tests and electron microscopy observation. The results show that −196 °C deformation produces a high dislocation density, which promotes the precipitation of the *T*1 phase and refines its sizes significantly. In addition, the grain boundary precipitates (GBPs) of −196 °C-stretched samples are suppressed considerably due to the high dislocation density in the grain interiors, which increases the ductility. In comparison, the strength remains nearly constant. Thus, it is indicated that cryogenic forming has the potential to provide the shape and property control for the manufacture of critical components of aluminum alloys.

Keywords: Al−Li alloy; cryogenic stretching; *T*1 phase; precipitation kinetics; grain boundary precipitates

---

1 Introduction

The 3rd Al−Li alloys have attracted great interest recently due to their low density, high specific stiffness, and strength [1]. The reported data suggest that adding 1 wt.% Li element in the alloy leads to a decrease in density by 3% and an increase in elastic modulus by 6% [2,3]. Low density and high strength enable Al−Li alloy to be applied extensively as structural materials [4] in the aerospace field to substitute 2219 alloys, such as the cryogenic fuel tanks of rockets [5].

Al−Li alloy is a type of age-strengthened aluminum alloy, and the strengthening effect depends largely on the precipitates formed during the aging process, mainly containing *T*1 (Al_2CuLi) phase, θ' (Al_2Cu) phase, and δ' phase (Al_3Li) [6,7]. The competing relationship among these phases is closely related to the minor alloying elements [8], such as Mg and Ag, the Cu/Li ratio [9], and the alloys' deformation and heat treatment. Many studies have demonstrated that cold working prior to aging treatment can effectively enhance the precipitation of the *T*1 phase in Al−Li alloys. In particular, the precipitation of θ' phase is restrained, and the microstructures are dominated by the *T*1 phase [10−12]. This phenomenon can be attributed to the high interfacial energy of the *T*1 phase, which renders its precipitation highly dependent on crystal defects. It is widely accepted that the *T*1 phase nucleates at dislocations. HOWE et al [13] proposed that the *T*1 phase can nucleate with the assistance of two Shockley partial dislocations on adjacent $\{111\}_{\alpha(\mathrm{Al})}$ planes. However, other nucleation sites for *T*1 phase have been consistently

---

Corresponding author: *Wei LIU, Tel: +86-451-86413115, E-mail: liuw@hit.edu.cn

https://doi.org/10.1016/S1003-6326(25)66947-0

Received 27 April 2024; accepted 10 January 2025

reported, including zirconium dispersion such as Al_3Zr [14,15], low angle grain boundaries [15], and octahedral voids/Guinier–Preston (GP) zones [16−18]. The GP zones for the *T*1 phase are reported to be enriched with Cu, Li, Mg, and Ag elements, which provide effective nucleation sites for the *T*1 phase [17,18]. In addition, the diameter of the *T*1 phase plays a decisive role in its strengthening effect due to the disc shape. RODGERS and PRANGNELL [19] found that even though the number density and volume fraction of the *T*1 phase increase with increasing stretching strain, the strengthening contribution from the *T*1 phase decreases. According to the modified precipitation strengthening model of the *T*1 phase [20,21], this can be attributed to the decrease in the diameter of the *T*1 phase.

Cryogenic forming technology for aluminum alloys has recently been implemented due to cooperative enhancements in ductility and strain hardening at cryogenic temperature (CT). Compared to RT stretching, CT stretching can induce changes in the dislocation configuration and density [22]. ZHEMCHUZHNIKOVA et al [23] observed uniform dislocation cells in the grain interiors after stretching at −196 °C, while the dislocation accumulated around grain boundaries after RT stretching. CHENG et al [24] further confirmed this phenomenon. They calculated the dislocation density, reporting a 12.6% increase in geometrically necessary dislocations (GND) density when stretching at −196 °C to a true strain of 0.09 compared to RT. As a result, the significant alteration in dislocation morphology after CT stretching can influence the precipitation behaviors and the mechanical properties of aluminum alloys. However, most previous studies have focused on the effect of RT pre-deformation. The mechanical properties and microstructure performance of the aluminum alloy that experienced CT deformation prior to aging have not been given enough attention. This matter has an essential impact on applying cryogenic temperature-forming technology for aluminum alloys. Although YE et al [25] have observed the *T*1 phase morphologies and mechanical properties of samples pre-stretched at both RT and −196 °C, there is a lack of a quantitative analysis of the effect of cryogenic deformation on the precipitation behaviors, including the precipitation kinetics of the *T*1 phase, the sizes of the GBPs and the matrix precipitates, as well as the mechanism of the precipitation distribution.

This work aims to investigate the effect of CT deformation prior to aging treatment on the precipitation kinetics of the *T*1 phase, sizes of the *T*1 phase and GBPs, and mechanical properties. Moreover, the strengthening and toughening mechanism of cryogenic pre-deformation was analyzed in depth by quantifying the contribution from each part. In addition, the relationship among the dislocation configuration, precipitate morphology, and mechanical properties was revealed.

2 Experimental

2.1 Materials preparation

The material utilized in this study is a 2195 Al−Li alloy plate provided by Jiangsu Haoran Spray Forming Co. Ltd., and the main chemical composition is listed in Table 1. The as-received plate has dimensions of 400 mm × 360 mm × 35 mm. The tested samples were cut from the plate at the same thickness. Figure 1 illustrates the microstructures of the as-received plate under hot extruded conditions. The inverse pole figure (IPF) (Figs. 1(a, b)) maps reveal a distinct ⟨111⟩ and ⟨100⟩ fiber texture aligned parallel to the extrusion direction (ED). The kernel average misorientation (KAM) (Fig. 1(c)) map indicates that slight local strains are present in the extruded plate.

Table 1 Chemical composition of 2195 Al−Li alloy (wt.%)

Cu	Li	Mg	Ag	Zr	Al
4.00	0.97	0.49	0.33	0.13	Bal.

2.2 Experimental procedures and mechanical property tests

The dog-bone-shaped tensile specimen has dimensions of 40 mm in the parallel gauge length, 10 mm in the gauge width, and a thickness of 1.5 mm. The length direction is aligned with the extrusion direction, while the width direction is aligned with the transverse direction. Figure 2(a) shows the experimental procedures; the specimens first underwent initial solution treatment followed by water quenching (WQ); the solution treatment in

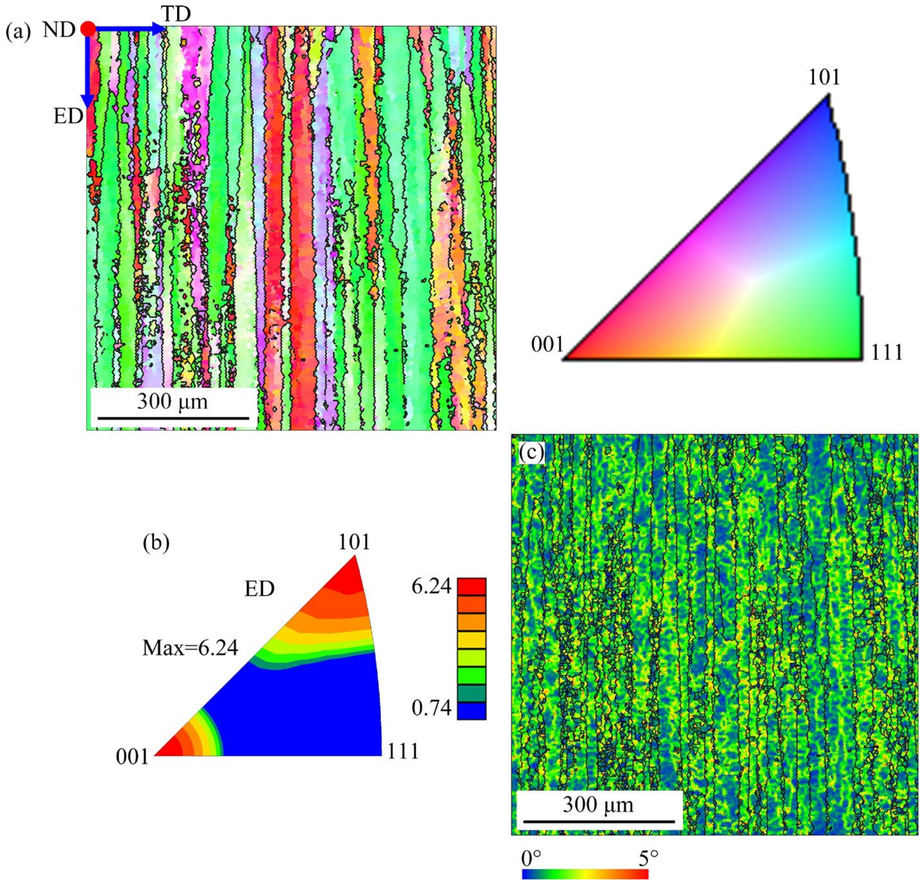

Fig. 1 Microstructures of extruded plate: (a, b) IPF maps; (c) KAM map

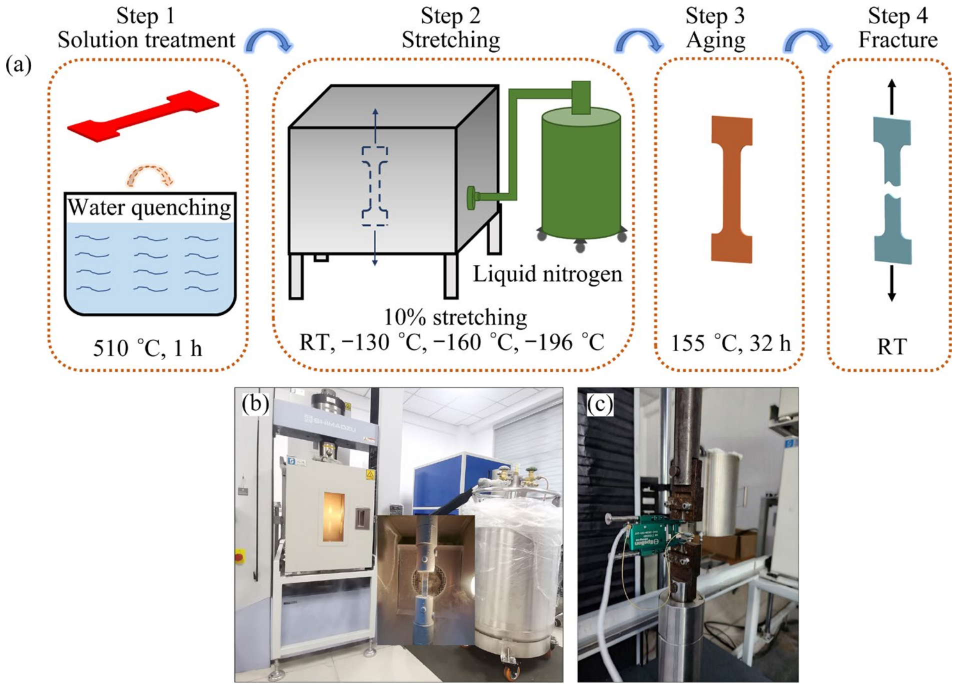

Fig. 2 Experimental procedure diagram (a) and experimental facilities (b, c)

all cases was conducted at 510 °C for 1 h. Subsequently, stretching was performed on each specimen using an electronic universal testing machine equipped with a controllable cryogenic temperature environment test chamber, as shown in Figs. 2(b, c). Each stretching process was completed within 5 min. The WQ-tempered specimens were promptly immersed in liquid nitrogen during the period between post-quenching and stretching to prevent natural aging effects, and the stretching was finished within 1 h of quenching for each set of experiments. Next, the stretched specimens were subjected to an aging treatment at 155 °C. Finally, fracture stretching tests were conducted at room temperature to obtain the mechanical properties. The temperature control in the chamber is highly accurate, as evidenced by the curves presented in Fig. 3. To ensure the credibility of the result, three samples were tested for each experimental parameter.

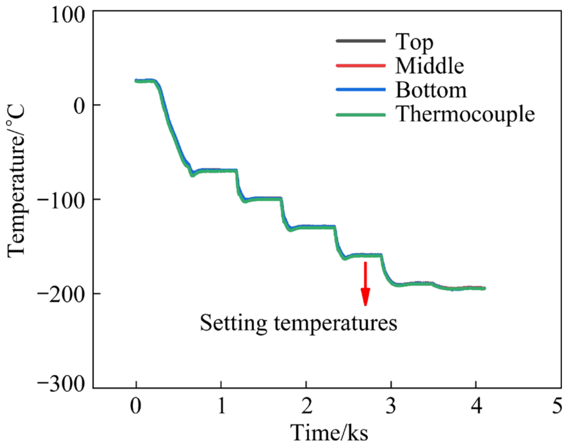

Fig. 3 Temperature test during cooling of chamber

Table 2 shows the experimental parameters, and two questions were investigated. First, the effect of stretching temperature prior to aging on the mechanical properties was studied. The WQ-tempered specimens were subjected to a 10% stretching strain at a strain rate of 0.001 s^{-1} and different temperatures (RT, −130 °C, −160 °C, −196 °C), then 32 h aging treatment at 155 °C was uniformly conducted. These samples were collectively referred to as LTS or LTSA, where A stands for aged state. Second, the influence of CT-stretching and aging duration on the mechanical properties was comprehensively investigated. The samples were stretched to 10% strain at RT and −196 °C, followed by an aging treatment at 155 °C for varying durations. These samples were collectively referred to as RTS(A) and CTS(A).

2.3 Microstructure characterization

The specimens utilized for microstructure characterization were all extracted from the central region of corresponding tensile samples, as shown in Fig. 4. To measure the volume fraction of *T*1 phases, DSC analysis was conducted using a STA449F3 instrument, with a heating rate of 10 °C/min ranging from 20 to 520 °C. Before measurement, sample mass was determined for normalization purposes, and the dimensions of the sample were adjusted to match the crucibles, with a diameter of 3 mm and a thickness of 1 mm. Samples for DSC analysis have been stretched at room temperature and −196 °C before aging treatment for varying durations.

The microstructures of aged samples and stretched WQ samples were observed using a Quanta 200FEG scanning electron microscope (SEM) equipped with an electron backscatter diffraction (EBSD) detector. Before observation, the EBSD samples were subjected to electrochemical polishing using a mixture of nitric acid and alcohol with volume ratio of 1:9. The samples were prepared using mechanical grinding and ion polishing techniques for bright field and high-resolution TEM imaging analysis. This was followed by an examination using Talos F200x transmission electron microscopy (TEM) to observe the precipitation behaviors. In addition, the lattice distortion of the samples after stretching at RT and −196 °C was characterized by X-ray diffraction (XRD) analysis by utilizing the X′PERT X-ray diffractometer equipped with Cu K_α radiation source of 0.15406 nm. Simultaneously, the modified Williamson−Hall XRD peak broadening analysis was used to measure the effect of the cryogenic deformation on the dislocation density [26].

Table 2 Experimental parameters of 2195 Al−Li alloy

Solution treatment	Uniaxial stretching		Aging treatment		Sample
	Amount/%	Temperature	Temperature/°C	Time/h	
(510 °C, 1 h) + water-quenching	10	RT, −130 °C, −160 °C, −196 °C	155	32	LTS(A)
	10	RT, −196 °C	155	0, 4, 8, 16, 24, 32, 48, 60	RTS(A), CTS(A)

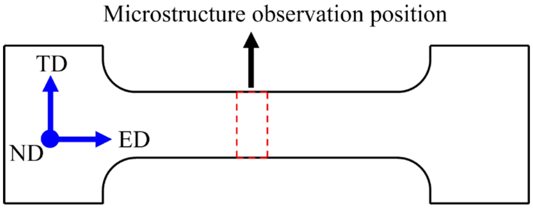

Fig. 4 Schematic diagram of interception position for microstructure observation specimen

3 Results

3.1 Quantitative analysis of precipitation kinetics

3.1.1 DSC curves analysis

The DSC curves, which are corrected according to Ref. [27], of RTS and CTS samples are presented in Fig. 5. These curves reveal the presence of two endothermic peaks, A1 and A2, as well as three prominent exothermic peaks, B1, B2, and B3. The small endothermic peak A1 observed below 230 °C can be attributed to the dissolution of GP zones formed at room temperature or in the early aging stage. The first exothermic peak, B1, occurring between 230 and 260 °C, is associated with *T*1 phase precipitation. In comparison, the second exothermic peak, B2, observed between 290 and 310 °C is related to *T*1 phase thickening, and the third exothermic peak, B3, appearing between 340 and 360 °C can be attributed to *θ*′ phase precipitation [27,28]. Additionally, the second endothermic peak A2 above 400 °C corresponds to the complete dissolution of all present precipitates within the sample.

3.1.2 Variation of T1 phase volume fraction with aging duration

To quantitatively investigate the specific effect of RT and CT stretching on the precipitation kinetics of the *T*1 phase, the volume fractions of the *T*1 phase after aging treatment of different durations were calculated using the methodology proposed by DORIN et al [27]. In particular, the normalized enthalpy is proportional to the volume fraction (f_v) of pre-existing *T*1 precipitates in samples before DSC measurement. The normalized enthalpy (ΔH) can be defined as an integral value of the thermal signal to temperature from the initial state until complete solid solution formation when the *T*1 phase is considered as the main precipitated phase, as shown in Eq. (1) [27]:

$$\Delta H=\frac{1}{\beta}\int_{100\ ^\circ\mathrm{C}}^{520\ ^\circ\mathrm{C}} Q_i(T)\,\mathrm{d}T \propto f_\mathrm{v}^{T1} \tag{1}$$

where β represents the heating rate of the DSC experiment, which was set to be 10 °C/min in this study, and $Q_i(T)$ is the thermal flow recorded during the experiment. The corrected DSC curves of RTSA and CTSA samples with various aging durations are depicted in Fig. 6. It can be observed that the intensity of the peak B1 decreases significantly with increasing the aging time, which indicates that the volume fraction of the pre-existing *T*1 precipitates

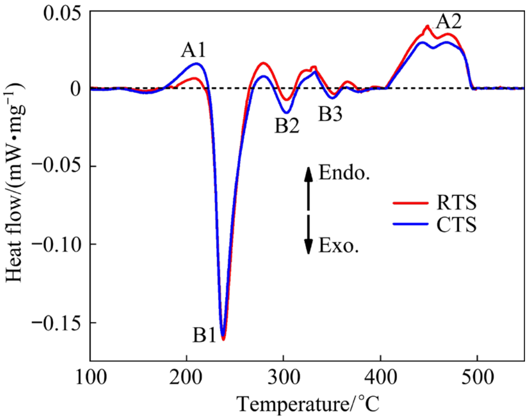

Fig. 5 DSC curves of RTS and CTS samples

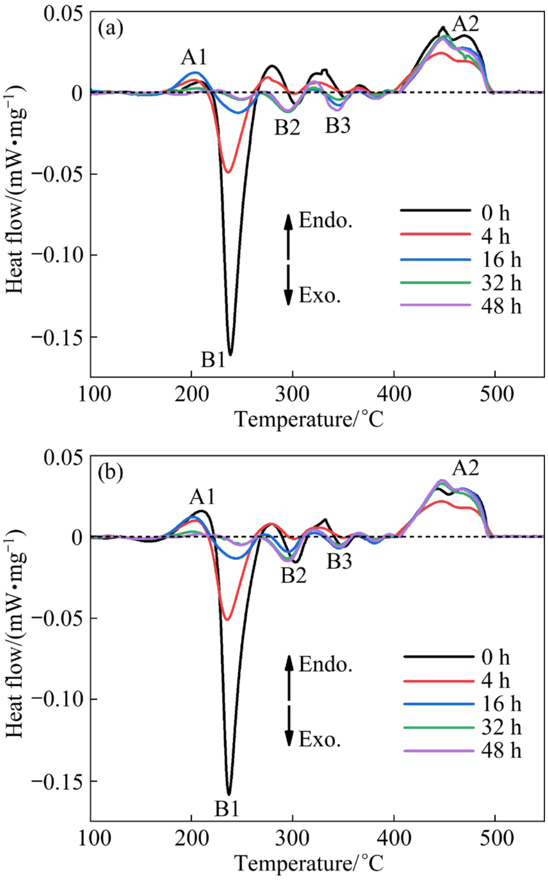

Fig. 6 DSC curves of RTSA (a) and CTSA (b) samples with varying aging durations

in the sample prior to DSC increases significantly. However, the peak B3 intensity change with aging time is much smaller than peak B1, indicating that the volume fraction of the θ' phase has little change with the aging time. Based on the few secondary phases in the WQ temper, the $T1$ phase precipitation dominated during precipitation. This view has been confirmed by DORIN et al [27]. Thus, the relationship in Eq. (1) can be applied in this study. The integration boundaries from 100 to 520 °C are consistent with those mentioned in Ref. [27].

The normalized enthalpy calculated according to Eq. (1) for each DSC curve in Fig. 6 is shown in Fig. 7(a). Then, the corresponding $T1$ phase volume fraction was subsequently determined using the correlation between normalized enthalpy and $T1$ phase volume fraction [27], as shown in Fig. 7(b). The results show that the $T1$ phase volume fraction increases with increasing aging time for both RTSA and CTSA samples, reaching a stable level after 16 h aging treatment. This is consistent with the precipitation kinetics curve obtained from in-situ SAXS measurements in Ref. [28]. It is observed that the rate of increase in f_V is nearly equal for both during the first 4 h of aging treatment. However, from 4 to 16 h, the increase rate of the CTSA sample surpasses that of the RTSA sample. The f_V of the RTSA sample ultimately stabilizes from 1.70% to 1.84%, whereas it ranges from 2.64% to 2.79% for the CTSA sample. The f_V of the CTSA sample with 32 h aging treatment exhibits a 43.5% increase compared to that observed in the RTSA sample. These findings suggest that stretching at −196 °C can significantly facilitate the precipitation of the $T1$ phase compared to stretching at RT.

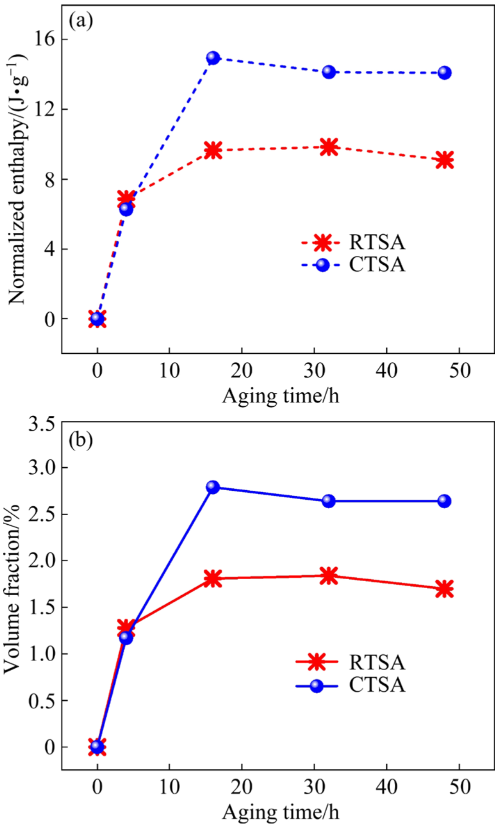

Fig. 7 Variation of normalized enthalpy (a) and $T1$ phase volume fraction (b) with aging time in RTSA and CTSA samples

3.1.3 Variation of GP zone content with aging duration

The endothermic peak A1, attributed to the dissolution of GP zones, indicates the presence of solute clusters prior to the DSC experiment. The reaction enthalpy (ΔH) of peak A1 is proportional to the constituent content of the GP zones formed before DSC tests. Figure 8 shows the variation in normalized ΔH for GP zone peaks with aging time.

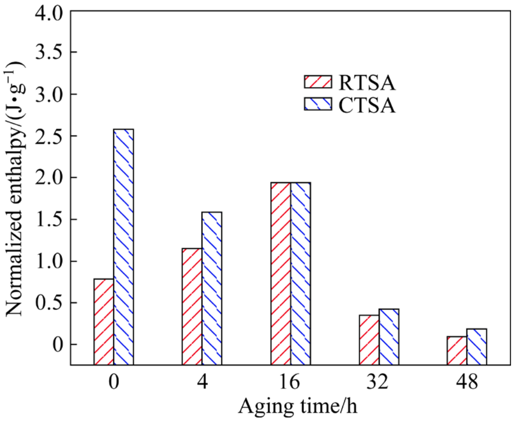

Fig. 8 Variation of normalized enthalpy of peak A1 with aging time in RTSA and CTSA samples

The initial GP zone content at 0 h in the CTSA sample is 3.29 times higher compared to the RTSA sample. This indicates that CT stretching significantly facilitates the formation of the GP zones. Moreover, the ΔH value of the CTSA sample exhibits a decreasing trend with increasing aging time, while it first increases and then decreases for the RTSA sample. The increase in the GP zones of the RTSA sample during the early aging stage can be attributed to the relatively lower kinetics of the $T1$ and θ' phases, which results in a reduced consumption of GP zones. The respective ΔH value of both samples almost reaches zero after 48 h aging treatment, indicating that most GP zones have transformed into other metastable or equilibrium phases during late-stage aging.

3.2 Distribution and morphology of precipitates

The SEM images in Figs. 9(a, b) depict grain boundary morphologies of RTSA and CTSA samples with a 32 h aging treatment, and many of bright white spots along the grain boundaries are observed. Energy dispersive spectrometer (EDS) analysis was performed on the bright white point A and the matrix point B, as shown in Figs. 9(c, d), respectively. The elemental composition illustrates that there is obvious enrichment of Cu element at the bright white point compared to the matrix material, which demonstrates that the bright white points can be attributed to GBPs. Notably, in RTSA sample (Fig. 9(a)), amounts of discontinuous and coarse rod-like or blocky precipitates are observed at grain boundaries. However, the GBPs are significantly suppressed in CTSA sample (Fig. 9(b)). The sizes of the GBPs were quantified by using the Image-Pro software, as shown in Figs. 10(a−c). And the volume fraction of the GBPs was determined by the ratio of the area of the bright white particles along the grain boundaries to the total area of the image. The length and width of the GBPs in CTSA sample are concentrated around the lower values compared to RTSA sample (Figs. 10(a, b)). Moreover, the mean values of the diameter, width, length of GBPs in CTSA sample are 2.72, 2.21, and 3.88 μm, respectively, which exhibits a decrease of 20%, 21% and 23% compared to RTSA sample. The volume fraction of the GBPs in RTSA and CTSA samples is 1.62% and1.24%, respectively, and the latter is 23% lower than the former.

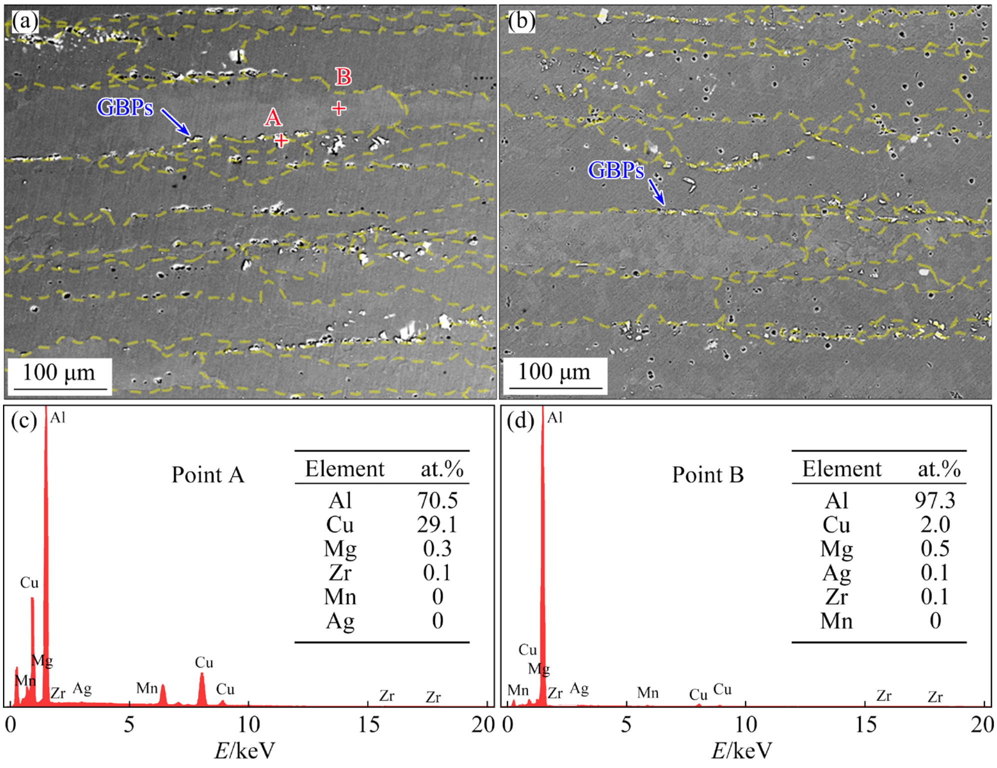

Element	at.%
Al	70.5
Cu	29.1
Mg	0.3
Zr	0.1
Mn	0
Ag	0

Element	at.%
Al	97.3
Cu	2.0
Mg	0.5
Ag	0.1
Zr	0.1
Mn	0

Fig. 9 SEM images of GBPs in RTSA (a) and CTSA (b) samples and EDS results of points A (c) and B (d)

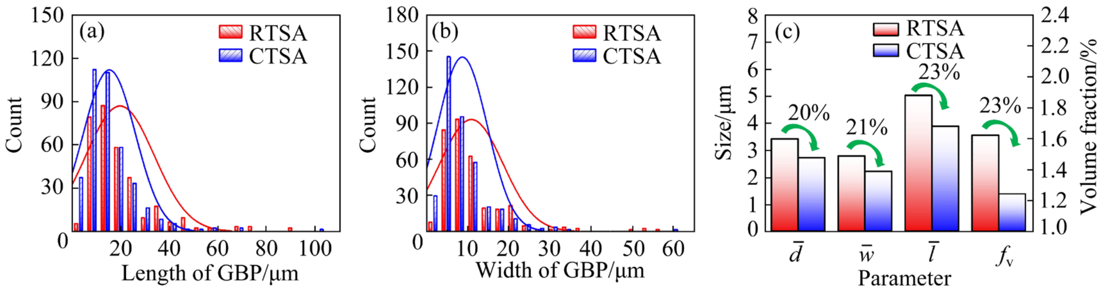

Fig. 10 Statistical analysis of GBPs in RTSA and CTSA samples: (a) Length distribution; (b) Width distribution; (c) Comparison of volume fraction (f_v) and mean values of diameter ($\bar{d}$), width ($\bar{w}$) and length ($\bar{l}$) of GBPs between RTSA and CTSA

The bright-field TEM images in Figs. 11(a, b) depict the morphologies within the matrix of the RTSA and CTSA samples with 32 h aging treatment. The beam directions are aligned along the $\langle 110\rangle_{\alpha(\mathrm{Al})}$ zone axis, which allows two distinct T1 plate phase variants to be observed on two $\{111\}_{\alpha(\mathrm{Al})}$ habit planes that are parallel to the $\langle 110\rangle_{\alpha(\mathrm{Al})}$ axis. One type of θ' plate precipitation variant on $\{200\}_{\alpha(\mathrm{Al})}$ habit planes can also be observed. The presence of the *T*1 phase is confirmed by the diffraction spots at 1/3 and 2/3$\{220\}_{\alpha(\mathrm{Al})}$, while diffraction spots at 1/2$\{200\}_{\alpha(\mathrm{Al})}$ provide evidence for the existence of θ' precipitates, although they appear less bright due to their smaller quantity. Through calibration, it is determined that two distinct *T*1 phase variants are precipitated on $(11\bar{1})_{\alpha(\mathrm{Al})}$ and $(111)_{\alpha(\mathrm{Al})}$ planes, respectively. The angle measurement between them precisely corresponds to the standard diffraction spot angle of 70.5°. This phenomenon strongly supports that the habit plane of *T*1 is $\{111\}_{\alpha(\mathrm{Al})}$. The diameter of the *T*1 phase within the matrix is measured from several images with a dimension of 262 nm × 262 nm, and the number of *T*1 phases to be counted in each sample is 100. The diameter distribution is illustrated in Fig. 12(a), revealing the average diameter of RTSA and CTSA samples as approximately 71.75 nm and 44.42 nm, respectively. Furthermore, it can be observed that the CTSA sample has more *T*1 phase inside grains.

The thickness of the *T*1 phase was also analyzed based on high-resolution TEM images, as depicted in Figs. 11(c, d). Representative images were selected for RTSA and CTSA samples. The measured thicknesses of the two *T*1 phases in the RTSA sample are 1.72 nm and 2.73 nm, respectively, while those in the CTSA sample are 0.99 nm and 2.21 nm, respectively. Twenty *T*1 phases were measured in each sample, and the thickness distribution is shown in Fig. 12(b). The average thicknesses of the *T*1 phase for RTSA and CTSA samples are determined to be 1.70 nm and 1.33 nm, respectively, representing a decrease of 21.8% in the *T*1 phase thickness for the CTSA sample compared to the RTSA sample.

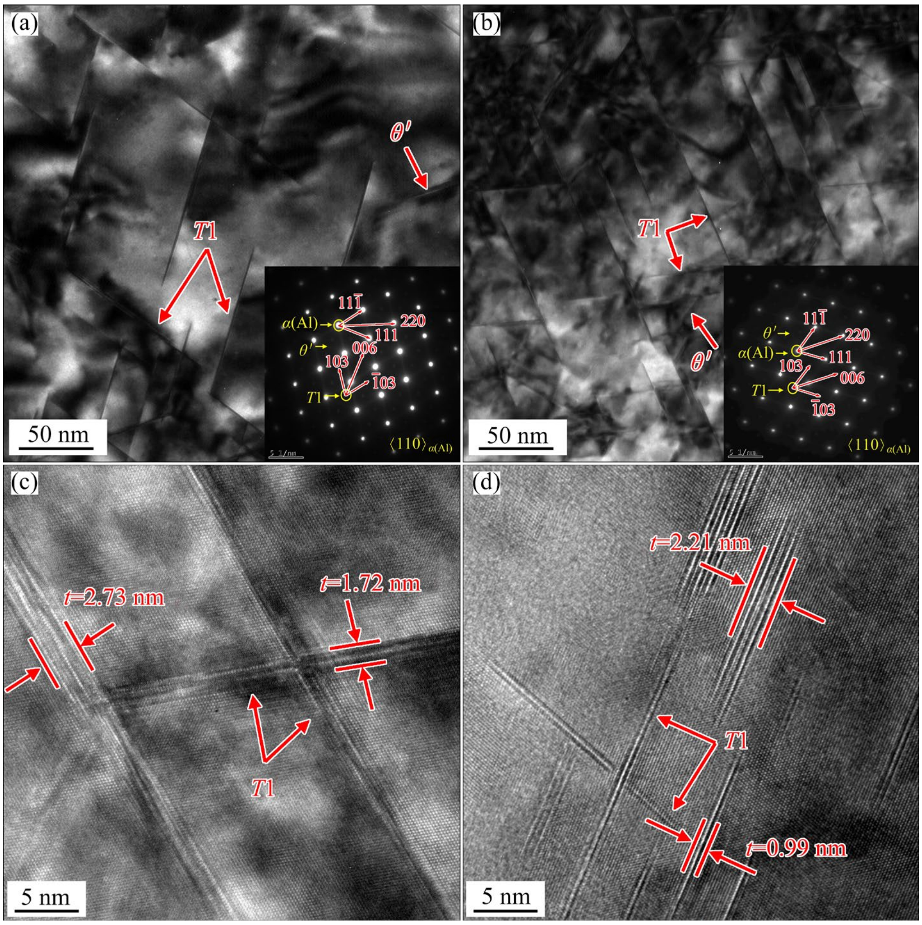

Fig. 11 TEM images of RTSA (a, c) and CTSA (b, d) samples after 32 h aging treatment: (a, b) Bright-field TEM images within matrix; (c, d) High-resolution TEM images of *T*1 phase

3.3 Mechanical properties

3.3.1 Effects of stretching temperature on mechanical properties

The mechanical properties of LTSA samples stretched at different temperatures are depicted in Fig. 13. The ultimate tensile strength (UTS) and yield strength (YS) slightly increase as the stretching temperature decreases. The UTS of the LTSA sample stretched at −196 °C is 576 MPa, 11 MPa higher than that at RT. The fracture elongation (EL) increases with decreasing the stretching temperature, as illustrated in Fig. 13(b). The EL of the LTSA sample stretched at −196 °C is 8.2%, 24.2% higher than that at RT.

3.3.2 Effects of cryogenic stretching on mechanical property response to aging duration

Figure 14 illustrates the UTS, YS, and EL of the RTSA and CTSA samples with various aging durations. The UTS and YS of RTSA samples increase with increasing aging time before 48 h,

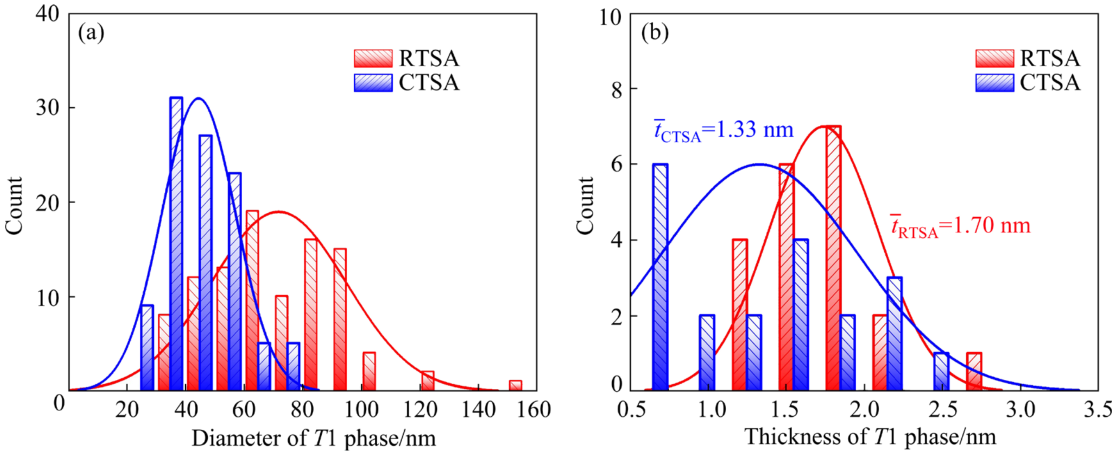

Fig. 12 Statistical analysis of $T1$ phase in RTSA and CTSA samples: (a) Diameter distribution; (b) Thickness distribution

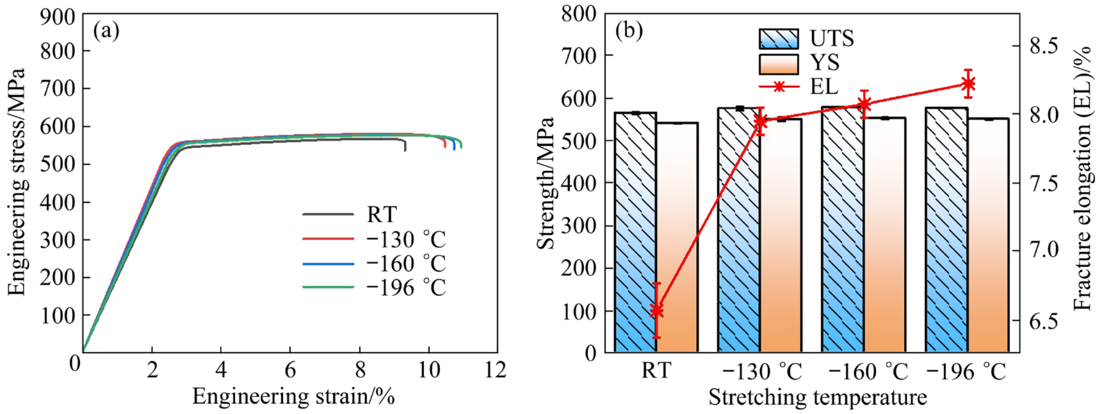

Fig. 13 Engineering stress−strain curves (a) and mechanical properties (b) of LTSA samples

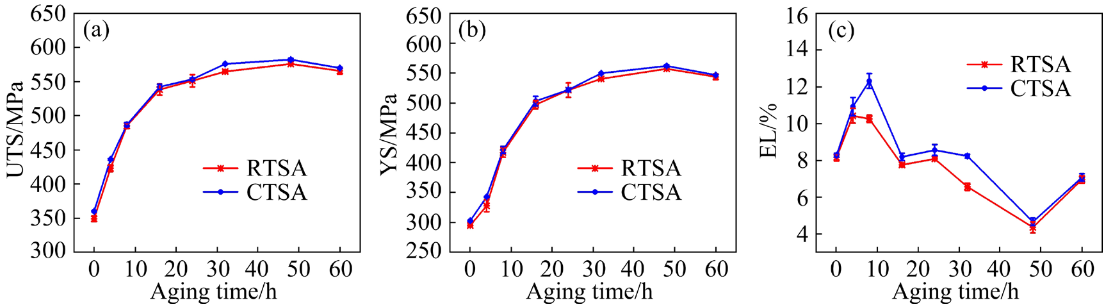

Fig. 14 Mechanical properties of RTSA and CTSA samples with different aging durations: (a) Ultimate tensile strength (UTS); (b) Yield strength (YS); (c) Fracture elongation (EL)

reaching the maximum values of 576 MPa and 558 MPa, respectively. Then, they decrease as the aging time increases to 60 h. The strength variation during aging of CTSA samples is almost identical to that of RTSA samples.

The EL variation during the aging of two samples is rather intricate. In the initial stage of aging treatment, the EL of both samples increases with aging time. The RTSA sample with 4 h aging treatment exhibits a maximum EL of 10.4%, and the maximum EL of 12.3% is achieved in the CTSA sample with 8 h aging treatment. The EL of both samples exhibits an initial drop at 16 h. Subsequently, the RTSA samples aged for 16−24 h maintain the EL within the range of 7.8%−8.2% before experiencing a significant decrease for the second time. In contrast, the CTSA samples aged for 16−32 h maintain the EL within the range of 8.2%−8.6%. Then, the elongations of RTSA and CTSA samples decrease again to their minimum values of 4.4% and 4.7%, respectively, when they are aged for 48 h, resulting from the coarsening and disappearance of some precipitates [29]. Further increase in aging time leads to a slight increase in EL, which may be attributed to the rise in recrystallization degree and the narrowing of the precipitate-free zone (PFZ) [29].

Generally, CTSA samples exhibit superior comprehensive mechanical properties compared to RTSA samples. On the one hand, the EL of the CTSA samples increases significantly, and their strength slightly improves compared to RTSA samples when they are aged for the same aging duration. The increase in EL is significant when the aging duration falls within 8−32 h. In particular, when the aging time increases from 8 to 32 h, the EL of CTSA samples increases in different degrees compared to RTSA samples under the same aging condition, and this increase ranges from 5.1% to 24.2%. On the other hand, compared with the RTSA sample, the CTSA sample can achieve superior comprehensive mechanical properties in a shorter aging period when they are aged at the same temperature. Specifically, the RTSA sample with 48 h aging treatment reaches the UTS of 576 MPa, the maximum strength throughout the aging process, while the EL is merely 4.4%. In contrast, the CTSA sample achieves the same UTS of 576 MPa but improved EL of 8.2%, after only 32 h aging treatment.

4 Discussion

4.1 Enhanced precipitation of *T*1 phase

Based on the analysis of DSC tests and the TEM images, the f_v of the T1 phase in the CTSA sample after 32 h aging treatment exhibits an increment of 43.5% compared to the RTSA sample with the same aging treatment. The average values of thickness and diameter decrease by 21.8% and 38.1%, respectively. Additionally, number density of the T1 phase can be determined by Eq. (2) [21]:

$$N=\frac{4f_v}{\pi t d^2} \tag{2}$$

where N, f_v, t, and d are the number density, volume fraction, thickness, and diameter, respectively. Based on the tested volume fraction and the mean values of thickness and diameter of the T1 phase, the number densities of T1 phase in RTSA and CTSA samples after 32 h aging treatment are determined to be 2.68×10^{21} and 1.28×10^{22} m^{-3}, respectively, according to Eq. (2). The number density of T1 phase in the CTSA sample exhibits a significant increment of 378% compared to the RTSA sample.

The enhancement of the GP zones after cryogenic deformation in the early aging stage can effectively reduce the nucleation difficulty and promote the precipitation of T1 phase. Moreover, the dislocation is also an essential factor that influences the precipitation of the T1 phase. Thus, the density and distribution of the dislocation after stretching at RT and −196 °C were obtained through EBSD and XRD, respectively. A high-resolution 2θ scan at a rate of 0.2 (°)/min was performed on the RTS and CTS samples to determine the dislocation density. As shown in Fig. 15, the centers of the (220) and (311) peaks in the CTS sample shift towards the higher values compared to the RTS sample, and the full width at half maximum (FWHM) values of (220) and (311) peak increases with the decrease of deformation temperature, which indicates that more lattice distortion has occurred in CTS sample.

The dislocation density was subsequently determined by applying a modified Williamson–Hall plot on XRD data. The relationship can be expressed by Eq. (3) [26]:

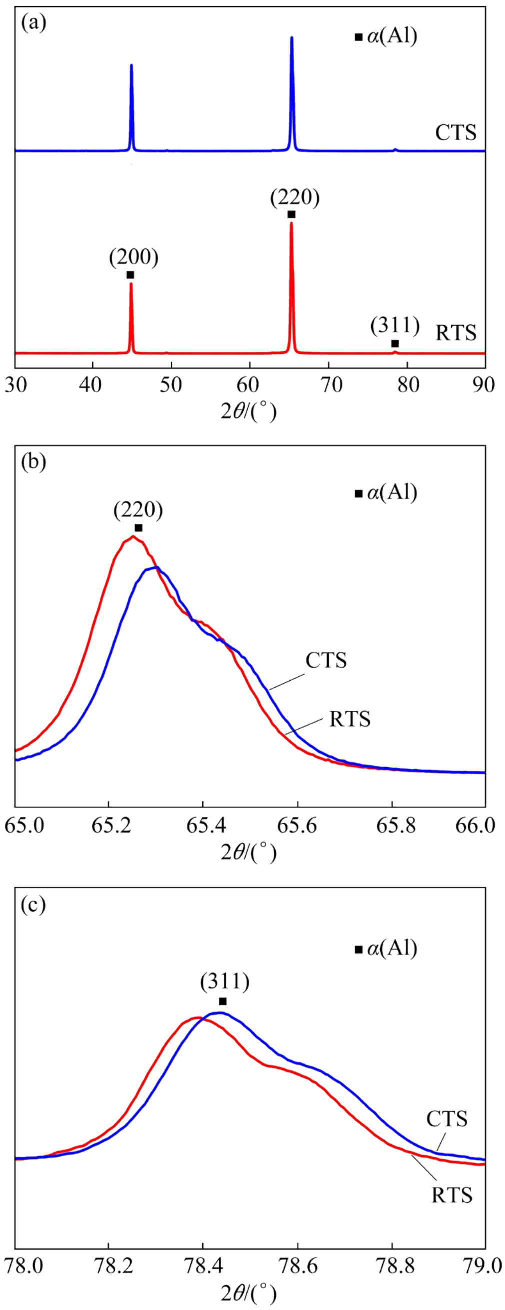

Fig. 15 XRD patterns of RTS and CTS samples: (a) Original XRD patterns; (b, c) Enlarged patterns around (220) and (311) peaks, respectively

$$\Delta K=(0.9/D)+\left(\frac{\pi M_{\mathrm{w}}b^2}{2}\right)\rho^{1/2}K^2\overline{C}_{hkl} \tag{3}$$

where ΔK is the strain-broadened FWHM in reciprocal space [30], D is the sub-grain size, b is the magnitude of burgers vector (0.286 nm for aluminum), M_{w} is the Wilkens arrangement parameter (M_{w}=2) [31], ρ is the dislocation density, K is the diffraction factor, and $\overline{C}_{hkl}$ is the average contrast factor for each specific plane (hkl). The values of the $\overline{C}_{hkl}$ for aluminum in {111}⟨110⟩ slip system can be calculated from the second-order elastic constants (C_{11}=107, C_{12}=61, and C_{44}=28 GPa) [32] with the help of the ANIZC program [33].

The fitting results of ΔK and K^2C are shown in Fig. 16, and the dislocation densities of RTS and CTS samples are determined to be 1.1×10^{14} and 1.6×10^{14} m^{-2}, respectively. The dislocation density of the CTS sample exhibits an increment of 45% compared to the RTS sample.

Figure 17 illustrates the distribution maps of geometrically necessary dislocations (GNDs) in samples stretched to 10% strain at RT and −196 °C, respectively. The GND density in the grain interiors is significantly enhanced in the CTS sample, and it reduces significantly around the grain boundary. In contrast, the distribution of the GND density in the RTS sample is the opposite, as illustrated by the red circles in Fig. 17(a) and the GND distribution of G1 and G2.

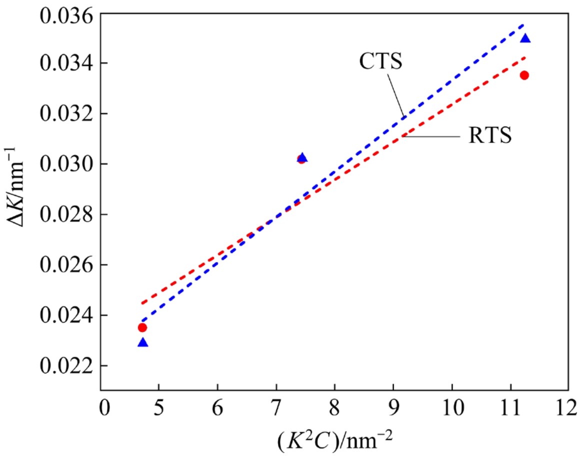

Fig. 16 Modified Williamson−Hall plots for RTS and CTS samples

Research by RODGERS and PRANGNELL [19] showed a near-linear increase in the dislocation density of both the T3 and T8 aged aluminum alloy with increasing pre-strain, demonstrating a low recovery level during the pre-straining. Moreover, the uniform increase in 'apparent' dislocation density of T8 temper alloys was observed compared to T3 temper, which was attributed to the introduction of matrix coherency strains from the precipitation of the $T1$ phase, and this suggests that the minimal static recovery occurred during the aging because it would be expected to reduce the dislocation density. In addition, MUKHOPADHYAY [34] found that

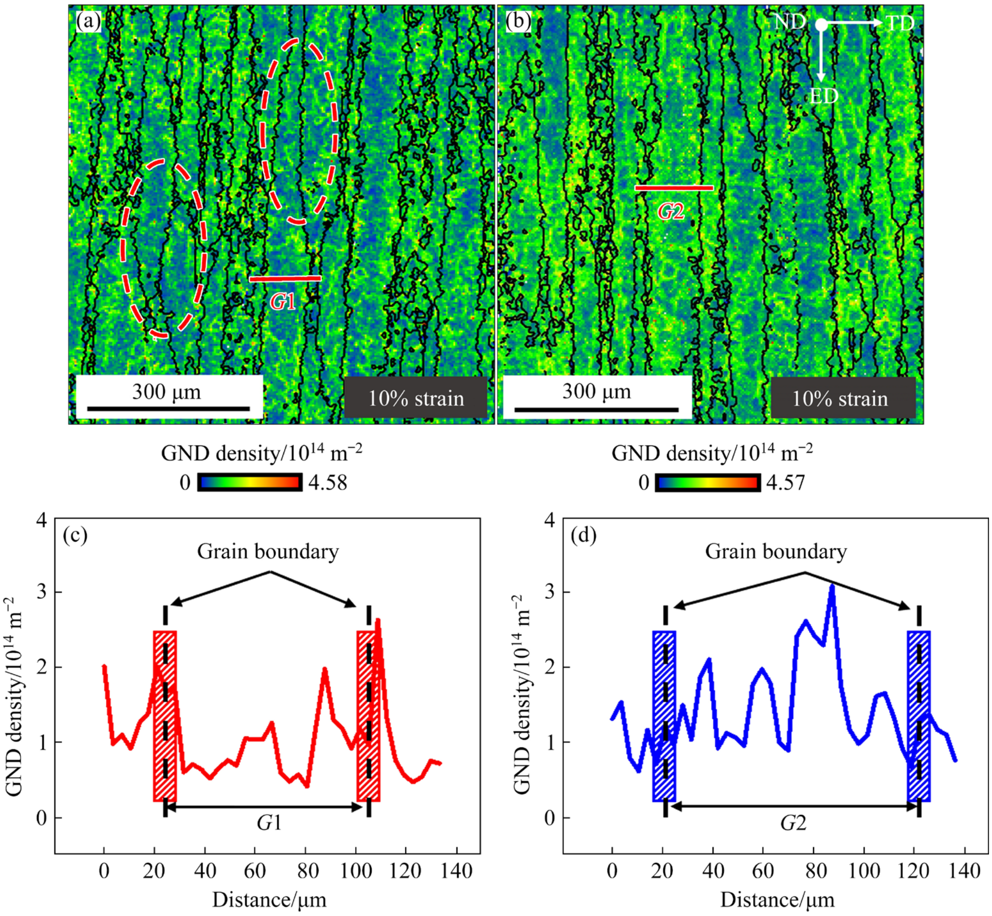

Fig. 17 GND distribution maps of samples stretched to 10% strain at RT (a, c) and −196 °C (b, d)

only at temperatures above 200 °C was the static recovery of dislocations in aluminum alloys appreciable during simulated annealing. Based on the investigations above, the dislocation recovery during the aging at 155 °C can be reasonably ignored in this study.

The dislocation density and GP zone content of the CTS sample exhibit an increment of 45% and 229% compared to the RTS sample, respectively. The dislocation defects accelerate solute atom diffusion rates and promote migration towards them because pipe diffusion is three orders of magnitude faster than bulk diffusion [35]. Moreover, the higher dislocation density after cryogenic deformation and more GP zones in an early aging stage in the CTS sample provide more nucleation sites for the $T1$ phase. This improves precipitation competitiveness of the $T1$ phase, leading to a decrease in diameter and thickness and an increase in the volume fraction and number density. In addition, enhanced dislocation density in the grain interiors after cryogenic stretching can promote the solute atom to diffuse towards the matrix.

4.2 Enhanced ductility

The mechanical property tests in Section 3.3 reveal that the ductility of LTSA samples exhibits an increasing trend as the stretching temperature decreases. Moreover, a consistent enhancement in ductility is observed for CTSA samples compared to RTSA samples when they were aged for the same duration. The enhanced ductility of CTSA samples can be attributed to the significant suppression of GBPs, as evidenced by SEM images (Fig. 9). In comparison to the RTSA sample, the mean values of the diameter, width, and length of GBPs in CTSA sample decrease by 20%, 21%, and 23%, respectively. The volume fraction decreases by 23% compared to the RTSA sample.

The fracture surface morphologies further support the suppressed GBPs in the CTSA sample. The fracture surface morphologies of RTSA and CTSA samples are shown in Fig. 18. There is a mixture of intergranular brittle fracture and dimple-type ductile fracture for both samples. However, an increased abundance of coarse rod-like secondary-phase particles is observed at the grain boundaries

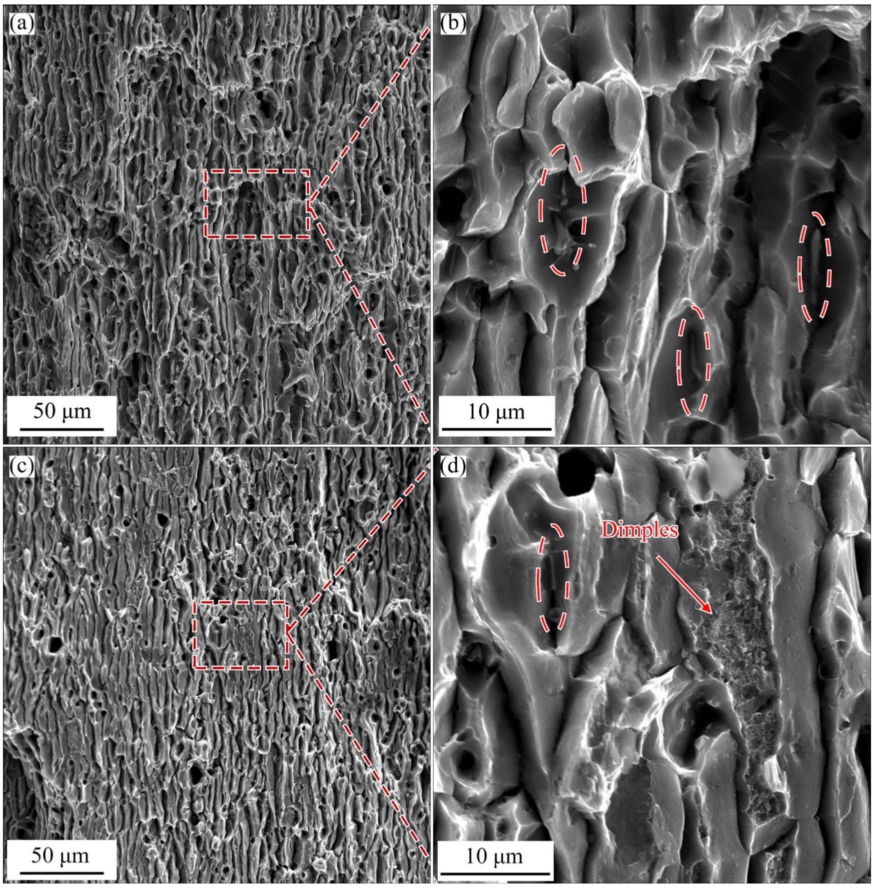

Fig. 18 Fracture surface morphologies of samples after 32 h aging treatment: (a, b) RTSA sample; (c, d) CTSA sample

in the RTSA sample, some of which are cracked. In contrast, precipitates at grain boundaries are significantly suppressed in the CTSA sample, and the size of the secondary-phase particles is reduced considerably. The coarse grain boundary precipitates can act as initiation sites for micro-cracks, propagating along the grain/sub-grain boundaries during stretching and contributing to intergranular fracture [36]. Thus, the GBPs enhance the degree of grain boundary cracking of the RTSA sample, resulting in a rougher fracture surface compared to the CTSA sample. Consequently, the suppression of GBPs in the CTSA sample decreases the micro-crack initiation sites and thus enhances the ductility.

The suppression of GBPs in CTSA samples can be attributed to a higher number of dislocations within the matrix, as depicted by Fig. 17. This reduces the diffusion kinetics of solute atoms towards grain boundaries, minimizing the gradient difference in supersaturation concentration between the matrix and grain boundaries. This results in enhanced precipitation within the matrix and suppressed precipitation at the grain boundary.

4.3 Analysis of strengthening and toughening mechanism

Based on the mechanical property results, the strength of the CTSA sample is marginally higher than that of the RTSA sample when they were aged for the same duration. The UTS and YS of the CTSA sample after 32 h aging treatment are 576 and 550 MPa, respectively, which increases by 11 and 9 MPa, respectively, compared to the RTSA sample after 32 h aging treatment. Although the refined $T1$ phase is expected to enhance the strength significantly, only a slight enhancement is observed.

In accordance with the research conducted by SHERCLIFF and ASHBY [37] and RODGERS and PRANGNELL [19], the primary strengthening mechanisms can be expressed using the following relationship:

$$\sigma_y=M_t(\tau_B+\Delta\tau_\rho+\Delta\tau_p) \quad (4)$$

where σ_y is the YS of material, M_t is the Taylor factor (typically considered to be 3.1 for fcc materials [38]), and τ_B is the base shear strength, comprising the intrinsic shear resistance of pure Al and solid solution strengthening. It can be reasonably assumed to remain constant during aging hardening due to the relatively minor change in base strength compared to the significant increase in strength resulting from precipitation [39]. $\Delta\tau_\rho$ and $\Delta\tau_p$ represent the increase in shear strength due to strain hardening and precipitation strengthening, respectively.

The method proposed by RODGERS and PRANGNELL [19] in their experimental work allows for separating the three components that contribute to strengthening. The base strength can be determined from the material immediately after solution treatment. At the same time, the strain hardening contribution can be obtained from the true stress−strain curve produced during stretching in the solution treatment status, as shown in Fig. 19. Finally, the increase in strength due to precipitation strengthening can be calculated by subtracting the base strength contribution and strain hardening contribution, which is reasonable because the slight static recovery occurs during artificial aging. Thus, any further increase in the temper yield stress can be attributed to the precipitation of the main strengthening *T*1 phase [19]. Based on above, the quantitative contributions from the *T*1 phase, strain hardening, and base strength to yield strength of the RTSA and CTSA samples are shown in Fig. 20. It is illustrated that the *T*1 phase contributes to yield strength most among the three main components for both RTSA and CTSA samples.

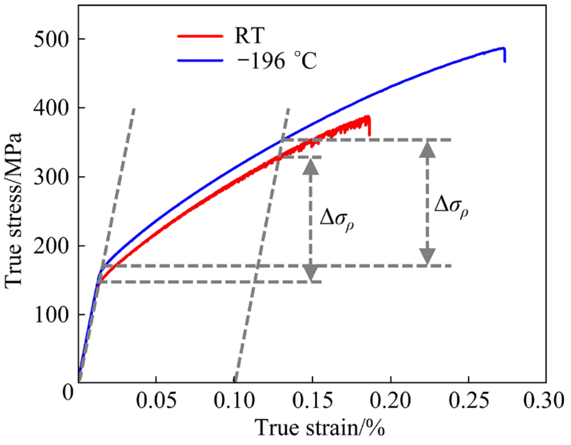

Fig. 19 True stress−strain curves of WQ-2195 Al−Li alloy at RT and CT to obtain strain hardening contributions

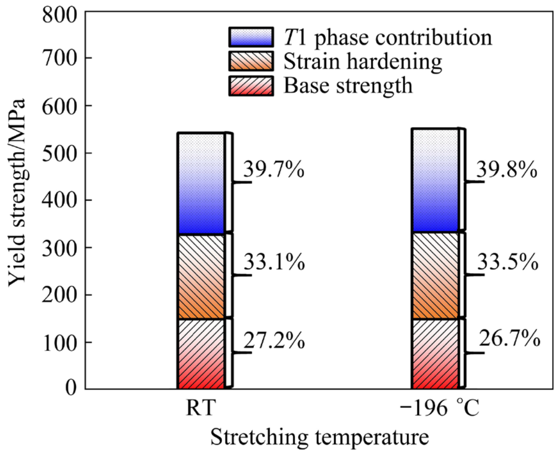

Fig. 20 Quantitative contributions from *T*1 phase, strain hardening, and base strength to yield strength of 2195 Al−Li alloy pre-stretched at RT and CT

The contribution from strain hardening to the yield strength can be expressed by the following relationship [40]:

$$\Delta\sigma_\rho=M_t\alpha\mu b\rho^{1/2} \tag{5}$$

where α is a dimensionless constant ranging from 0.2 to 0.5 [41], and μ is the shear modulus. Based on the results shown in Fig. 17, it can be observed that the CTSA sample exhibits an increase of 45% in GND density compared to the RTSA sample. Consequently, the increase of the contribution from strain hardening to yield strength in the CTSA sample is higher than that of the RTSA sample.

Table 3 lists the diameter, thickness, volume fraction, and number density of *T*1 phase in RTSA and CTSA samples, where the number density is determined according to Eq. (2). DORIN et al [21] has previously noted that the precipitation-induced shear strength increment shows a positive correlation with diameter and number density but a negative correlation with thickness of *T*1 phase, i.e., $\Delta\tau\propto d^2N^{1/2}t^{-2/3}$. The *T*1 phase of the CTSA sample exhibits a pronounced increase in the f_v and number density and a substantial reduction in the mean values of thickness and diameter compared to the RTSA sample. Therefore, it is necessary to further estimate the combined influence of *T*1 phase

Table 3 Characteristics of *T*1 phase for RTSA and CTSA samples after 32 h aging treatment

Sample	f_v/%	t/nm	d/nm	N/m^{-3}
RTSA	1.84	1.70	71.75	2.68×10^{21}
CTSA	2.64	1.33	44.42	1.28×10^{22}

morphology on the contribution of precipitation strengthening by considering all factors.

When predicting the precipitation strengthening contribution of the *T*1 phase, researchers have proposed two models based on the Orowan by-passing mechanism and shearing mechanism, respectively. Two models were compared and it is found that the model based on the shearing mechanism provides more accurate predictions than the model based on the Orowan by-passing mechanism [42]. This model maintains a consistently high prediction accuracy before and around peak aged status. The difference between two models is attributed to the transformation from the shearing mechanism to the by-passing mechanism of the *T*1 phase [43−45]. Based on these investigations, DORIN et al [21] modified Nie and Muddle's model based on the shearing mechanism by considering stacking fault energy, which is associated with shearing a precipitate besides the interfacial energy. The validated model can be expressed as

$$\Delta\tau_{\mathrm{p}}=\frac{1.211d\gamma_{\mathrm{eff}}^{3/2}}{t^{2}}\sqrt{\frac{bf_{\mathrm{v}}}{\Gamma}} \tag{6}$$

$$\gamma_{\mathrm{eff}}=\gamma_{\mathrm{i}}+\left(\frac{t}{2b\cos\varphi\sin\theta}-\frac{1}{2}\right)\gamma_{\mathrm{SF}} \tag{7}$$

where γ_i and γ_{SF} are the interfacial energy and stacking fault energy, respectively, Γ represents the dislocation line tension in the matrix. The values of γ_i and γ_{SF} obtained are 0.085 J/m^2 and 0.005 J/m^2, respectively. Figure 21 illustrates the combined contribution from *T*1 phase strengthening to YS as predicted by Eq. (6). The calculated contribution to yield strength from *T*1 phase strengthening in the CTSA sample is 226 MPa, which is only 23 MPa higher than that in the RTSA sample with the same aging duration. The experimentally measured value of the *T*1 phase strengthening in the CTSA sample is 4 MPa higher than that of the RTSA sample, according to Fig. 20. Therefore, both experimental and computational results show that the increase of the *T*1 phase strengthening in the CTSA sample is un-conspicuous. The increase in the volume fraction and number density, as well as the decrease in the thickness of the *T*1 phase for the CTSA sample, can enhance its strengthening effect. However, the decrease in the diameter of the *T*1 phase weakens its obstruction effect on the dislocation slip. The disk-like shape of the *T*1 phase results in a more significant effect on particle strength due to decreased diameter. Thus, the effect of the decrease in diameter on strengthening counteracts that of the increase in obstacle density on the slip plane.

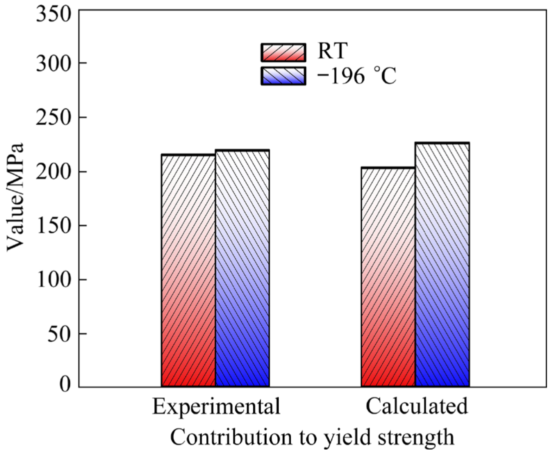

Fig. 21 Effect of stretching temperature on contribution from *T*1 phase to yield strength of 2195 Al−Li alloy

According to the abovementioned analysis, Fig. 22 presents an analysis of the strengthening and toughening mechanisms of 2195 Al−Li alloy after deformation and aging treatment. When the stretching is conducted at −196 °C, the dislocation is mainly concentrated in the grain interiors, and more GP zones are formed. When the same stretching is performed at RT, the dislocation is primarily focused around the grain boundary, and the GP zone content is significantly reduced. The more the intragranular dislocations, the easier the diffusion of solute atoms toward the grain interiors during the aging process, which can relatively restrain the precipitation around the grain boundary. As the number of solute atoms in the material is certain at the same aging equilibrium state, the increased intragranular dislocations in the CTS sample can effectively suppress the formation of grain boundary precipitates (GBPs). The coarse GBPs can easily lead to crack initiation around the grain boundary [36]; thereby, the suppressed GBPs in the CTSA sample can reduce the formation of cracks, enhancing the plasticity. Meanwhile, the higher dislocation density after −196 °C deformation and the increased content of GP zones in the CTS sample can effectively refine the *T*1 phase and increase its number density, thus maintaining its strength.

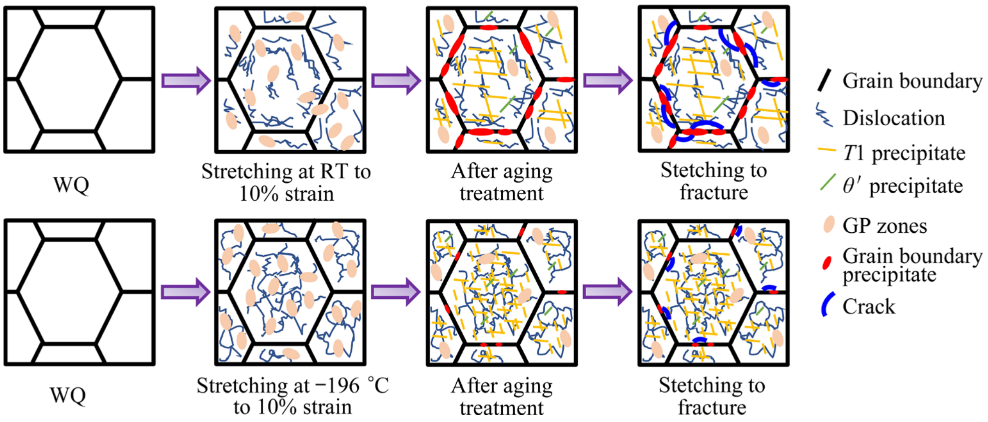

Fig. 22 Comparison of effect of stretching at RT and −196 °C on strengthening and toughening mechanism of 2195 Al−Li alloy

5 Conclusions

(1) Cryogenic deformation prior to aging can significantly enhance the ductility of 2195 Al−Cu−Li alloy compared to RT deformation, but the strength is not reduced. The elongation of the CTSA sample after 32 h aging treatment reaches 8.2%, 25.3% higher than that of the RTSA sample.

(2) The GBPs of the CTSA sample are significantly suppressed compared to the RTSA sample. This reduces the micro-crack initiation and enhances the ductility. The intragranular dislocation density after −196 °C deformation increases, facilitating the diffusion of solute atoms towards the grain interiors and inhibiting the formation of the precipitates around the grain boundary.

(3) The cryogenic deformation produces higher dislocation density and promotes the formation of more GP zones. This enhances the precipitation kinetics of the *T*1 phase in the CTSA sample and refines its size. The number density, average diameter, and thickness of the *T*1 phase in the CTSA sample after 32 h aging treatment are $1.28\times10^{22}\ \mathrm{m}^{-3}$, 44.42 nm, and 1.33 nm, respectively.

(4) The effect of the decrease in diameter of the *T*1 phase on strengthening counteracts that of the increase in obstacle density on the slip plane, and thus, the precipitation strengthening effect from the *T*1 phase after −196 °C deformation is not significantly enhanced compared to the RT deformation.

CRediT authorship contribution statement

Meng-jia YAO: Investigation, Methodology, Writing − Original draft & editing; **Hua-bo ZHOU:** Conceptualization, Writing − Review & editing; **Rui-qian WANG:** Writing − Review & editing, Project administration; **Wei LIU:** Data curation, Writing − Review & editing, Funding acquisition, Project administration.

Declaration of competing interest

The authors declare that they have no known competing financial interests or personal relationships that could have appeared to influence the work reported in this paper.

Acknowledgments

This work was financially supported by the National Key Research and Development Program of China (No. 2019YFA0708801) and the National Natural Science Foundation of China (No. 51875125).

References

[1] DAI Xiang, SHI Lei, TIAN Chun-yan, WU Chuan-song, GAO Song. Effect of ultrasonic vibration on microstructures and mechanical properties of friction stir welded 2195 Al−Li alloy [J]. Transactions of Nonferrous Metals Society of China, 2024, 34: 80−93.

[2] LAVERNIA E J, SRIVATSAN T S, MOHAMED F A. Strength, deformation, fracture behaviour and ductility of aluminium−lithium alloys [J]. Journal of Materials Science, 1990, 25: 1137−1158.

[3] FU Rong, HUANG Yuan-chun, LIU Yu, LI Hui, WANG Zhi-wen. Influence of homogenization treatment on microstructure and recrystallization behavior of 2195 Al−Li alloy [J]. Transactions of Nonferrous Metals Society of China, 2023, 33: 2255−2271.

[4] MENG Zi-jie, ZHANG Cun-sheng, WU Cheng-ge, ZHANG Hao, CHEN Liang, ZHAO Guo-qun, YAN Hai. Low cycle fatigue behavior and fatigue life prediction of 2195 Al−Li

alloy at warm temperatures [J]. Transactions of Nonferrous Metals Society of China, 2023, 33: 2574−2587.

[5] LI Hui, WANG Zhi-wen, FU Rong, HUANG Yuan-chun. Influence of aging treatment on corrosion behavior of extruded 2195 Al−Li alloy [J]. Transactions of Nonferrous Metals Society of China, 2024, 34: 755−768.

[6] YANG Xing-hai, WANG Jun-sheng, WANG Shuo, LI Xing-xing, XUE Cheng-peng, TIAN Guang-yuan, ZHANG Yu-xuan, KE Yu-bin, XIE Zhen-hua. Quantifying the kinetics of δ' precipitates in a novel Al−Li−Cu−Mg alloy during two-step aging by small-angle neutron scattering [J]. Materials Science and Engineering A, 2023, 872: 144963.

[7] ZHAO Xin-yue, LIU Wen-sheng, XIAO Dai-hong, MA Yun-zhu, HUANG Lan-ping, TANG Ya. A critical review: Crystal structure, evolution and interaction mechanism with dislocations of nano precipitates in Al−Li alloys [J]. Materials & Design, 2022, 217: 110629.

[8] DESCHAMPS A, GARCIA M, CHEVY J, DAVO B, DE GEUSER F. Influence of Mg and Li content on the microstructure evolution of AlCuLi alloys during long-term ageing [J]. Acta Materialia, 2017, 122: 32−46.

[9] DECREUS B, DESCHAMPS A, DE GEUSER F, DONNADIEU P, SIGLI C, WEYLAND M. The influence of Cu/Li ratio on precipitation in Al−Cu−Li−x alloys [J]. Acta Materialia, 2013, 61: 2207−2218.

[10] HAN Jia-qiang, WANG Hui-ming, XU Ai-jun, NIU Kang-min. Enhanced matrix precipitation of T1 (Al_2CuLi) phase in AA2055 Al−Li alloy during stress aging process [J]. Materials Science and Engineering A, 2021, 827: 142057.

[11] WANG Yong-xiao, MA Xin-wu, XI Hua-kun, ZHAO Guo-qun, XU Xiao, CHEN Xiao-xue. Effects of pre-stretching and aging treatments on microstructure, mechanical properties, and corrosion behavior of spray-formed Al−Li alloy 2195 [J]. Journal of Materials Engineering and Performance, 2020, 29: 6960−6973.

[12] LI Jin-feng, YE Zhi-hao, LIU Dan-yang, CHEN Yong-lai, ZHANG Xu-hu, XU Xiu-zhi, ZHENG Zi-qiao. Influence of pre-deformation on aging precipitation behavior of three Al−Cu−Li alloys [J]. Acta Metallurgica Sinica (English Letters), 2016, 30: 133−145.

[13] HOWE J M, LEE J, VASUD VAN A K. Structure and deformation behavior of T1 precipitate plates in an Al−2Li−1Cu alloy [J]. Metallurgical Transactions A, 1988, 19: 2911−2920.

[14] ITOH G, CUI Q, KANNO M. Effects of a small addition of magnesium and silver on the precipitation of T1 phase in an Al−4%Cu−1.1%Li−0.2%Zr alloy [J]. Materials Science and Engineering: A, 1996, 211: 128−137.

[15] ARAULLO-PETERS V, GAULT B, GEUSER F D, DESCHAMPS A, CAIRNEY J M. Microstructural evolution during ageing of Al−Cu−Li−x alloys [J]. Acta Materialia, 2014, 66: 199−208.

[16] GAO Zhen, LIU Ji-zi, CHEN Jiang-hua, DUAN Shi-yun, LIU Zi-ran, Ming Wen-quan, WU Cui-lan. Formation mechanism of precipitate T1 in AlCuLi alloys [J]. Journal of Alloys and Compounds, 2015, 624: 22−26.

[17] DENG Yan-jun, BAI Jian-hui, WU Xiao-dong, HUANG Guang-jie, CAO Ling-fei, HUANG Li. Investigation on formation mechanism of T1 precipitate in an Al−Cu−Li alloy [J]. Journal of Alloys and Compounds, 2017, 723: 661−666.

[18] MA Juan, LIU Xiao-chun, YAN De-sheng, RONG Li-jian. A novel GP-Li precursor and the correlated precipitation behaviors in Al−Cu−Li alloys with different Cu/Li ratio [J]. Acta Materialia, 2023, 243: 118442.

[19] RODGERS B I, PRANGNELL P B. Quantification of the influence of increased pre-stretching on microstructure-strength relationships in the Al−Cu−Li alloy AA2195 [J]. Acta Materialia, 2016, 108: 55−67.

[20] NIE J F, MUDDLE B C. Microstructural design of high-strength aluminum alloys [J]. Journal of Phase Equilibria, 1998, 19: 543−551.

[21] DORIN T, DESCHAMPS A, GEUSER F D, SIGLI C. Quantification and modelling of the microstructure/strength relationship by tailoring the morphological parameters of the T1 phase in an Al−Cu−Li alloy [J]. Acta Materialia, 2014, 75: 134−146.

[22] DENG Yan-jun, HUANG Guang-jie, CAO Ling-fei, WU Xiao-dong, HUANG Li, XIA Ming-yong, LIU Qing. Improvement of strength and ductility of Al−Cu−Li alloy through cryogenic rolling followed by aging [J]. Transactions of Nonferrous Metals Society of China, 2017, 27: 1920−1927.

[23] ZHEMCHUZHNIKOVA D, MOGUCHEVA A, KAIBYSHEV R. Mechanical properties and fracture behavior of an Al–Mg–Sc–Zr alloy at ambient and subzero temperatures [J]. Materials Science and Engineering A, 2013, 565: 132−141.

[24] CHENG Wang-jun, LIU Wei, FAN Xiao-bo, YUAN Shijian. Cooperative enhancements in ductility and strain hardening of a solution-treated Al−Cu−Mn alloy at cryogenic temperatures [J]. Materials Science and Engineering A, 2020, 790: 139707.

[25] YE Fan, YU You-xing, ZHANG Bao-shuai, RONG Jian, HE Dong-lei, HAN Bao-shuai, MA Xiao-guang, ZENG Yuan-song, XU Yan-jin, WU Su-jun. Influence of pre-stretching at ambient and cryogenic temperatures on dislocation configuration, precipitation behaviour, and mechanical properties of 2195 Al−Cu−Li alloy [J]. Journal of Materials Research and Technology, 2023, 22: 2983−2995.

[26] UNGAR T. Dislocation densities, arrangements and character from X-ray diffraction experiments [J]. Materials Science and Engineering A, 2001, 309/310: 14−22.

[27] DORIN T, DESCHAMPS A, DE GEUSER F, LEFEBVRE W, SIGLI C. Quantitative description of the T1 formation kinetics in an Al−Cu−Li alloy using differential scanning calorimetry, small-angle X-ray scattering and transmission electron microscopy [J]. Philosophical Magazine, 2014, 94: 1012−1030.

[28] GUMBMANN E, DE GEUSER F, SIGLI C, DESCHAMPS A. Influence of Mg, Ag and Zn minor solute additions on the precipitation kinetics and strengthening of an Al−Cu−Li alloy [J]. Acta Materialia, 2017, 133: 172−185.

[29] CHEN Xiao-xue, MA Xin-wu, XI Hua-kun, ZHAO Guo-qun, WANG Yong-xiao, XU Xiao. Effects of heat treatment on the microstructure and mechanical properties of extruded 2196 Al−Cu−Li alloy [J]. Materials & Design, 2020, 192: 108746.

[30] KREETHI R, MISHRA S K, MONDAL A K, DUTTA K. On the comparative assessment of ratcheting-induced dislocation

density in 42CrMo4 steel by X-ray diffraction profile analysis and hardness measurement [J]. Philosophical Magazine, 2018, 98: 2637−2656.

[31] SUGIYAMA S, OGAWA T, HE L, WANG Z, ADACHI Y. Quantitative analysis of the recovery process in pure iron using X-ray diffraction line profile analysis [J]. Materials, 2021, 14: 895.

[32] LASKA A, SZKODO M, CAVALIERE P, MOSZCZYŃSKA D（in Polish）, MIZERA J. Analysis of residual stresses and dislocation density of AA6082 butt welds produced by friction sir welding [J]. Metallurgical and Materials Transactions A, 2023, 54: 211−225.

[33] RIBARIK G, UNGAR T. Computer program ANIZC for the calculation of diffraction contrast factors of dislocations in elastically anisotropic cubic, hexagonal and trigonal [J]. Journal of Applied Crystallography, 2003, 36: 160−162.

[34] MUKHOPADHYAY P. Quantified static recovery trend of constricted jogs of aluminium alloys during annealing. [J]. Defence Science Journal, 2021, 71: 822−825.

[35] XIAO Han, ZHANG Kai-feng, SHI Cheng-cheng, LU Zhen, JIANG Ju-fu. Influence of electropulsing treatment combined with pre-deformation on ageing behavior and mechanical properties of 5A90 Al−Li alloy [J]. Journal of Alloys and Compounds, 2019, 784: 1234−1247.

[36] LANG Yu-jing, ZHOU Gu-xin, HOU Long-gang, ZHANG Ji-shan, ZHUANG Lin-zhong. Significantly enhanced the ductility of the fine-grained Al–Zn–Mg–Cu alloy by strain-induced precipitation [J]. Materials & Design, 2015, 88: 625−631.

[37] SHERCLIFF H R, ASHBY M F. A process model for age hardening of aluminium alloys—I. The model [J]. Acta Metallurgica et Materialia, 1990, 38: 1789−1802.

[38] STARINK M J, WANG S C. A model for the yield strength of overaged Al–Zn–Mg–Cu alloys [J]. Acta Materialia, 2003, 51: 5131−5150.

[39] HUANG Y, ROBSON J D, PRANGNELL P B. The formation of nanograin structures and accelerated room-temperature theta precipitation in a severely deformed Al−4wt.%Cu alloy [J]. Acta Materialia, 2010, 58: 1643−1657.

[40] MARTIN J W. The strength of aged alloys [M]//Precipitation Hardening. 2nd ed. Oxford: Butterworth-Heinemann, 1998: 79−125.

[41] MADEC R, DEVINCRE B, KUBIN L P. From dislocation junctions to forest hardening [J]. Physical Review Letters, 2002, 89: 255508.

[42] ZHU A W, CHEN J, STARKE E A. Precipitation strengthening of stress-aged Al–*x*Cu alloys [J]. Acta Materialia, 2000, 48: 2239−2246.

[43] DESCHAMPS A, DECREUS B, DE GEUSER F, DORIN T, WEYLAND M. The influence of precipitation on plastic deformation of Al–Cu–Li alloys [J]. Acta Materialia, 2013, 61: 4010−4021.

[44] CSONTOS A A, STARKE E A. The effect of inhomogeneous plastic deformation on the ductility and fracture behavior of age hardenable aluminum alloys [J]. International Journal of Plasticity, 2005, 21: 1097−1118.

[45] NIE J F, MUDDLE B C. On the form of the age-hardening response in high strength aluminium alloys [J]. Materials Science and Engineering A, 2001, 319/320/321: 448−451.

2195 Al−Li 合金超低温变形和时效后 *T*1 相析出行为及力学性能的定量分析

姚梦佳 [1,2]，周华博 [1,2]，王睿乾 [1,2]，刘 伟 [1,2]

1. 哈尔滨工业大学 金属精密热加工全国重点实验室，哈尔滨 150001；
2. 哈尔滨工业大学 材料科学与工程学院，哈尔滨 150001

摘 要：对淬火态 2195 Al−Li 合金在室温至−196 ℃不同温度下进行拉伸，研究超低温变形对时效析出行为和力学性能的影响。通过差示扫描量热(DSC)测试和电镜观察，研究了 *T*1 相的析出动力学和峰时效态的显微组织。结果表明：−196 ℃变形时产生较高的位错密度，促进了 *T*1 相的析出并使其尺寸明显细化；此外，−196 ℃拉伸后试样的晶内位错密度较高，使得晶界析出相(GBPs)明显受到抑制，从而提高了塑性，而强度几乎保持不变。因此，低温成形技术具有为铝合金关键部件的制备提供形状和性能控制的潜力。

关键词：铝锂合金；超低温拉伸；*T*1 相；析出动力学；晶界析出相

(Edited by Bing YANG)